

A parametric study of the coalescence of liquid drops in a viscous gas

Sprittles, James; Shikhmurzaev, Yulii

DOI:
[10.1017/jfm.2014.362](https://doi.org/10.1017/jfm.2014.362)

License:
None: All rights reserved

Document Version
Publisher's PDF, also known as Version of record

Citation for published version (Harvard):
Sprittles, J & Shikhmurzaev, Y 2014, 'A parametric study of the coalescence of liquid drops in a viscous gas', *Journal of Fluid Mechanics*, vol. 753, pp. 279–306. <https://doi.org/10.1017/jfm.2014.362>

[Link to publication on Research at Birmingham portal](#)

Publisher Rights Statement:
© 2014 Cambridge University Press
Permitted under CUP policy at time of publication.

General rights

Unless a licence is specified above, all rights (including copyright and moral rights) in this document are retained by the authors and/or the copyright holders. The express permission of the copyright holder must be obtained for any use of this material other than for purposes permitted by law.

- Users may freely distribute the URL that is used to identify this publication.
- Users may download and/or print one copy of the publication from the University of Birmingham research portal for the purpose of private study or non-commercial research.
- User may use extracts from the document in line with the concept of 'fair dealing' under the Copyright, Designs and Patents Act 1988 (?)
- Users may not further distribute the material nor use it for the purposes of commercial gain.

Where a licence is displayed above, please note the terms and conditions of the licence govern your use of this document.

When citing, please reference the published version.

Take down policy

While the University of Birmingham exercises care and attention in making items available there are rare occasions when an item has been uploaded in error or has been deemed to be commercially or otherwise sensitive.

If you believe that this is the case for this document, please contact UBIRA@lists.bham.ac.uk providing details and we will remove access to the work immediately and investigate.

A parametric study of the coalescence of liquid drops in a viscous gas

James E. Sprittles[†] and Yulii D. Shikhmurzaev

Mathematics Institute, University of Warwick, Coventry CV4 7AL, UK

School of Mathematics, University of Birmingham, Birmingham B15 2TT, UK

(Received 25 February 2014; revised 16 April 2014; accepted 22 June 2014;
first published online 22 July 2014)

The coalescence of two liquid drops surrounded by a viscous gas is considered in the framework of the conventional model. The problem is solved numerically with particular attention paid to resolving the very initial stage of the process which only recently has become accessible both experimentally and computationally. A systematic study of the parameter space of practical interest allows the influence of the governing parameters in the system to be identified and the role of viscous gas to be determined. In particular, it is shown that the viscosity of the gas suppresses the formation of toroidal bubbles predicted in some cases by early computations where the gas' dynamics was neglected. Focusing computations on the very initial stages of coalescence and considering the large parameter space allows us to examine the accuracy and limits of applicability of various 'scaling laws' proposed for different 'regimes' and, in doing so, reveal certain inconsistencies in recent works. A comparison with experimental data shows that the conventional model is able to reproduce many qualitative features of the initial stages of coalescence, such as a collapse of calculations onto a 'master curve' but, quantitatively, overpredicts the observed speed of coalescence and there are no free parameters to improve the fit. Finally, a phase diagram of parameter space, differing from previously published ones, is used to illustrate the key findings.

Key words: breakup/coalescence, capillary flows, drops and bubbles

1. Introduction

When two drops of the same liquid come into contact, a coalescence process merges the two distinct bodies of liquid into one, after which the resulting single body evolves towards its equilibrium shape (figure 1). This process can be observed in a range of natural phenomena and holds the key to a vast number of emerging technologies such as the '3D printers' used to additively manufacture complex products by assembling liquid microdrops in '2D slices' (Derby 2010) or the coalescence-induced jumping mechanism being harnessed to enhance the heat transfer properties of a solid covered by a condensed liquid (Enright *et al.* 2012). Although the equilibrium configuration of such systems is sometimes known, the dynamics of the process that leads to it is not always well understood. An example of unexpected dynamic behaviour is the repeated

[†] Email address for correspondence: J.E.Sprittles@warwick.ac.uk

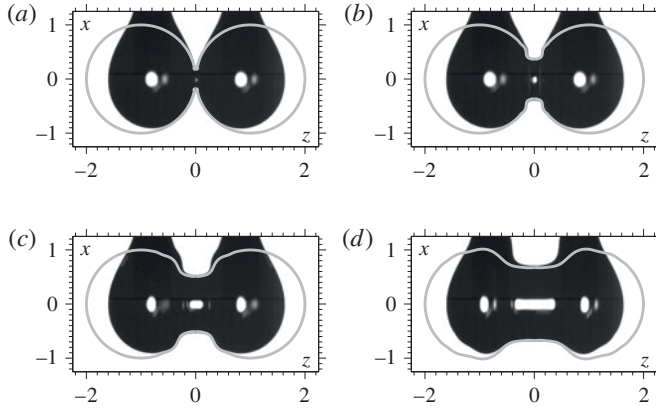


FIGURE 1. Comparison of our coalescence computations with free spheres in the inertial regime, against experiments in Paulsen *et al.* (2012) conducted using 1 mm radii pendant drops of silicone oil with $Re = 1.9 \times 10^4$. The dimensionless time t_i is based on the inertial scale: (a) $t_i = 0.01$; (b) $t_i = 0.07$; (c) $t_i = 0.15$; (d) $t_i = 0.3$. As can be seen, the neck region is accurately described far beyond the initial stages of the process even though the global geometry is different.

partial coalescence of an ever-decreasing sized drop with a liquid bath, the so-called ‘coalescence cascade’, observed by ultra-high-speed imaging techniques (Thoroddsen & Takehara 2000).

Although improving optical techniques have made it possible to study small-scale high-speed free-surface flows (Thoroddsen, Etoh & Takehara 2008), they have intrinsic limitations associated with their spatial resolution and, in particular, are unable to resolve the cusp-like region formed when two drops are pressed into one another, or when one drop is pressed into a solid (Eddi, Winkels & Snoeijer 2013). As a result, one can often only observe the appearance of the bridge between the two drops when it has already travelled $\sim 10\%$ of the initial drop radius, i.e. long after what one would class as the initial stages of coalescence as such, where the merging of the two liquid bodies into one has already occurred. An alternative technique, based on measuring the electrical resistance of the bridge connecting the drops, has been applied in Paulsen, Burton & Nagel (2011), Paulsen *et al.* (2014) where, for the first time, the submicrometre scales of the coalescence phenomenon have been resolved. This offers a unique opportunity to compare the predictions of the conventional model, i.e. the incompressible Navier–Stokes equations and standard kinematic and dynamic boundary conditions with the surface tension of the liquid–gas interface assumed constant, which are known to be singular for this problem (Eggers, Lister & Stone 1999), with the new experiments for the initial stages of the coalescence phenomenon at unprecedentedly small spatiotemporal scales.

In a recent publication (Sprittles & Shikhmurzaev 2012a), the coalescence of liquid drops in an inviscid dynamically passive gas, henceforth referred to as a ‘passive gas’, was computed in the framework of two different mathematical models by adapting a finite-element code initially developed for dynamic wetting phenomena (Sprittles & Shikhmurzaev 2012b,c, 2013). The results were compared with experiments from both electrical measurements in Paulsen *et al.* (2011) and optical measurements in Thoroddsen, Takehara & Etoh (2005). The first model examined was the conventional

one used in most studies, e.g. in Eggers *et al.* (1999), and the one considered in this work. Its essence is that after the two drops touch at a point, it is assumed that an infinitesimal but somehow smooth liquid bridge is formed that connects them, so that the coalescence as such is actually over. The model is concerned with the subsequent process, namely how the Laplacian capillary pressure due to the highly curved free surface drives the already formed single body of liquid towards its equilibrium shape. The results of our numerical computations (Sprittles & Shikhmurzaev 2012a) showed that the conventional model of the coalescence phenomenon, whose solution is known to contain singularities in, amongst other things, the radial velocity at the start of the process (Hopper 1984, 1990; Richardson 1992; Hopper 1993a,b), overshoots experimental data from Paulsen *et al.* (2011), i.e. it overpredicts the speed at which coalescence occurs, whilst a singularity-free model, incorporating interface formation dynamics (Shikhmurzaev 2007), captures the data more accurately. This model has recently been the subject of further, more detailed, investigation in Sprittles & Shikhmurzaev (2014a).

Notably, in Sprittles & Shikhmurzaev (2012a) the main emphasis was on a direct comparison between the two aforementioned models and experimental data. In contrast, here our attention will be focused entirely on the conventional model, which, so far, remains the most popular approach to describe such flows, with computations resolving both the fine scales associated with the initial bridge propagation right through to the scales on which the overall dynamics of the coalescing drops comes into play. In particular, we will report on the results of a full parametric study of the coalescence process which allowed us to: (a) determine the role of parameters in the model; (b) identify different ‘regimes’ proposed in the published literature and the crossovers between them; and (c) calculate the accuracy of ‘scalings’ proposed for these regimes. As a result of the comprehensive comparison between our computations and previous theoretical works on the coalescence phenomenon we will identify a number of discrepancies in the previous published literature.

Furthermore, given that, as shown in Sprittles & Shikhmurzaev (2012a), the conventional model overpredicts the speed of coalescence compared with data from experiments, where the exterior fluid was air, i.e. a viscous gas, one could argue that the overshoot could, perhaps, be attributed to the neglect of the gas’ dynamics. For example, one may argue that the high pressures needed to squeeze the gas out of the cusp-like region at the bridge front, if accounted for in the model, could slow the front down. Therefore, in the present paper, we also include two-phase calculations of the coalescence phenomenon into our parametric study and make a direct comparison of the results to the experimental data.

2. Asymptotic results and ‘scaling laws’ for the coalescence of liquid drops

Simplified expressions for the coalescence event which are valid in different ‘regimes’, have gained popularity due to their simplicity compared with the full-scale theoretical description for, in particular, providing explicit formulas to fit experimental data. On the theoretical level, in the framework of the conventional model, the most commonly used results are those in Hopper (1984), where conformal mapping techniques have been used to derive an exact solution to the problem of two-dimensional viscous-dominated coalescence. On the level of the scaling laws, the most frequently used ones were derived in Eggers *et al.* (1999), for both viscous- and inertia-dominated coalescence. The recent results in Paulsen *et al.* (2012) suggest the existence of a third inertially limited viscous (ILV) regime which precedes all others. The results of these works will be subject to scrutiny in the forthcoming sections, and are therefore now briefly described.

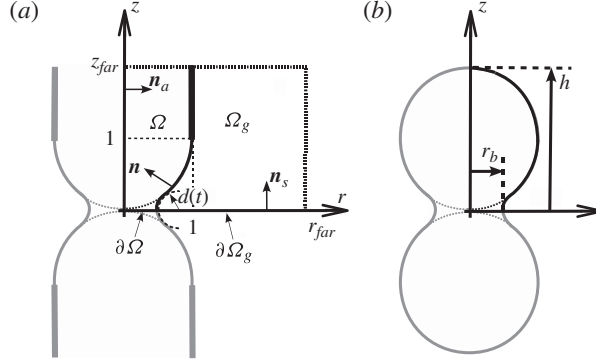


FIGURE 2. A definition sketch for the coalescence of two identical ‘pinned hemispheres’ grown from syringes (a) and a sketch of coalescing ‘free spheres’ (b) showing the bridge radius r_b and apex height h . In the results section, the bridge radius will simply be denoted as r .

2.1. Viscous-dominated regime

The natural scale for velocity in this regime is given by $U_v = \sigma/\mu$, where μ is the liquid’s viscosity and σ is the surface tension of the liquid–gas interface, so that the capillary number $Ca = \mu U_v/\sigma = 1$. The appropriate timescale is then $T_v = R\mu/\sigma$, where R is the drop’s initial radius, which is the characteristic length scale in all regimes. The Reynolds number then becomes $Re = \rho\sigma R/\mu^2$, where ρ is the liquid’s density. Alternatively, some works, e.g. Paulsen *et al.* (2012), characterise the coalescence in terms of the Ohnesorge number which is related to the Reynolds number by $Oh = Re^{-1/2}$. Henceforth, unless denoted by a subscript ‘dim’ to denote ‘dimensional’, all quantities will be assumed dimensionless.

2.1.1. Exact solution in Hopper (1984)

The exact result obtained in Hopper (1984) gives the entire two-dimensional shape of two coalescing identical cylindrical drops, described by Stokes flow, in a passive gas as a function of time. What will be of most interest to us in characterising the coalescence event are the bridge radius r and height of the drops h (figure 2) as a function of time t , which are given by

$$r = \sqrt{2}(1-m)(1+m^2)^{-1/2}, \quad h = \sqrt{2}(1+m)(1+m^2)^{-1/2} \quad (2.1a,b)$$

where the parameter m is related to the time by

$$t = \frac{\pi\sqrt{2}}{4} \int_{m^2}^1 [\tau(1+\tau)^{1/2}K(\tau)]^{-1} d\tau, \quad K(\tau) = \int_0^1 [(1-x^2)(1-\tau x^2)] dx, \quad (2.2)$$

an expression which can easily be evaluated numerically.

2.1.2. Scaling law in Eggers *et al.* (1999)

The scaling laws in Eggers *et al.* (1999) are derived by balancing the driving capillary pressure $\sigma\kappa$, where κ is the curvature at the bridge front, with the key resistive mechanism, i.e. either viscous or inertial forces. In both cases, the driving

force is shown to result primarily from the longitudinal curvature so that $\kappa \propto 1/d(t)$, where $d(t)$ is the longitudinal radius of curvature at the bridge front (figure 2).

In the viscous-dominated case, it is shown that, local to the bridge front for $r \ll 1$, the two-dimensional solution from Hopper (1984) can be used to provide the radius of curvature, which scales like r^α , where $\alpha = 3$. In other words, it is assumed that the evolution of 2D and 3D drops are identical in the initial stages. It is then further argued that $\alpha = 3/2$ when the gas has some viscosity μ_g .

As a result, the expression for the (dimensionless) bridge radius for $r \ll 1$ has the form

$$r = -C_v t \ln t, \quad C_v = \frac{(\alpha - 1)}{2\pi}, \quad \alpha = \begin{cases} 3, & \bar{\mu} = 0; \\ 3/2, & \bar{\mu} > 0. \end{cases} \quad (2.3)$$

Notably, and somewhat counter-intuitively, when the external fluid is regarded to be viscous, the form of (2.3) does not depend on the gas-to-liquid viscosity ratio $\bar{\mu} = \mu_g/\mu$, and it is only α which changes from 3 to 3/2, although it is specified in Eggers *et al.* (1999) that the region of applicability of the formula should depend on this parameter; (2.3) is expected to hold for $r < \bar{\mu}^{2/3}$.

2.2. Inertia-dominated regime

The characteristic scale for velocity in the inertia-dominated regime is obtained by setting the Weber number to unity, so that $U_i = \sqrt{\sigma/(\rho R)}$. The characteristic timescale for this regime is then given by $T_i = \sqrt{\rho R^3/\sigma}$. The Reynolds number in the inertia-dominated regime Re_i is related to that in the viscous regime Re by $Re_i = Re^{1/2}$.

In Eggers *et al.* (1999), it is suggested that the driving capillary pressure due to the surface tension and based on the longitudinal curvature obtained from the undisturbed free-surface shape of the drops $d(t) \sim r_{dim}^2(t_{dim})/R$ is balanced by the dynamic pressure $\rho(dr_{dim}/dt_{dim})^2$. As a result, one has $r_{dim}/R = C_i(t_{dim}/T_i)^{1/2}$, where C_i is a constant of proportionality, so that, once non-dimensionalised by our characteristic scales in this regime, the scaling law takes the form

$$r = C_i t_i^{1/2} \quad (2.4)$$

where t_i is time made dimensionless by T_i .

Notably, in contrast to (2.3), there is no closed-form expression for $r(t)$, as the expression contains an unknown prefactor. These issues are addressed in further detail in Sprittles & Shikhmurzaev (2014b).

2.3. ILV regime

Recently, an ILV regime has been shown in Paulsen *et al.* (2012), through a combination of experimental and computational techniques, to precede either the viscosity-dominated regime or the inertia-dominated one, for non-zero values of Re , see also Paulsen (2013), Paulsen *et al.* (2014). In particular, it is noted that in Hopper's exact solution (2.1), for Stokes flow, once coalescence commences, the entire volume of each drop is translated towards the other, so that the motion cannot be considered as 'local' to the neck region, as in (2.3) and (2.4). Such global motion can be observed, for example, by measuring the height of the drops, i.e. a position far away from the bridge, as a function of time.

In Paulsen *et al.* (2012), it is shown that for finite Re the neck must reach a finite radius before it has enough force to create this global motion; until it does so, it is in the ILV regime. Experiments suggest that in this regime the bridge propagates at a constant speed, which is simply determined from dimensional analysis to be U_v . This gives

$$r = C_v t \quad (2.5)$$

where, in contrast to (2.3), C_v is an *a priori* unknown prefactor.

3. Overview of the study

Although many experimental and theoretical studies have considered the various regimes, and the crossovers between them, there has been no systematic parametric study of the system using a full-scale theoretical description accounting for viscous, inertial and capillary effects as well as the influence of the ambient fluid surrounding the coalescing drops. Furthermore, computations have tended to either focus on only the very initial stages of the process, often using boundary integral methods to look only at the viscous regime (Eggers *et al.* 1999) or the inertial one (Oguz & Prosperetti 1989; Duchemin, Eggers & Josserand 2003), or on the global dynamics, with the initial stages not considered. As a result, in none of these works has the influence of a viscous gas been considered in detail. It is this gap in the theoretical research on coalescence which we shall now address and, as a by-product, uncover and examine various inconsistencies in the published literature.

In §4, the problem formulation is given for both the case of free spheres coalescing as well as the pinned hemispherical drop configuration often considered experimentally (figure 2). Section 5 describes the main elements of our computational approach including, when required, references to more detailed expositions. Results are presented in §6, where a full systematic study of parameter space is performed which elucidates, in particular, the effect of both the liquid's and the outer gas' properties. At each stage, a detailed comparison with the previous literature, summarised in §2, is provided. The full parametric study is followed by a comparison with experimental results both from qualitative and quantitative perspective in §7. The results from §§6 and 7 are tied in with the published literature in §8, where it proves illustrative to represent our findings with a phase diagram. Final conclusions and, motivated by our results, suggestions for new directions of experimental and theoretical research are given in §9.

4. Problem formulation

Two different geometries will be considered in this work (figure 2) both regarding the axisymmetric coalescence of liquid drops formulated in the standard way. The majority of calculations will be for the typical experimental set-up in which hemispherical drops are grown from syringes and surrounded by a viscous gas but at certain points we will also be compelled to study the case of coalescing free spheres.

It has previously been demonstrated that, for the parameter regimes considered, in the initial stages of coalescence the effects of gravity can be ignored (Sprittles & Shikhmurzaev 2012a), so that the problem becomes symmetric and can be reduced to determining the motion of one drop in the (r, z) -plane of a cylindrical coordinate system with the symmetry conditions on the $z = 0$ plane at which the drops initially touch (figure 2). The syringe, when considered, is taken to be a semi-infinite cylinder with zero-thickness walls located at $r = 1$, $z > 1$ which separates the liquid phase

$r < 1$ from the gas $r > 1$, where the lengths are scaled with the radius of each drop R . The precise far field conditions, i.e. those associated with the syringe head, have a negligible effect on the initial stages of coalescence (Sprittles & Shikhmurzaev 2012a).

Both fluids, i.e. the liquid forming the drops and the ambient gas, are considered to be incompressible and Newtonian with constant densities ρ , ρ_g and viscosities μ , μ_g . As before and henceforth, the subscript g refers to properties of the gas. The fluids occupy domains Ω and Ω_g , respectively (figure 2). To non-dimensionalise the system of the governing equations for the bulk variables, we use the drop radius R as the characteristic length scale, U_v as the scale for velocities, T_v as the timescale and σ/R as the scale for pressure. Then, the continuity and momentum balance equations in the two phases take the form

$$\nabla \cdot \mathbf{u} = 0, \quad Re \left[\frac{\partial \mathbf{u}}{\partial t} + \mathbf{u} \cdot \nabla \mathbf{u} \right] = \nabla \cdot \mathbf{P}; \quad \mathbf{P} = -p\mathbf{I} + [\nabla \mathbf{u} + (\nabla \mathbf{u})^T], \quad \mathbf{r} \in \Omega \quad (4.1a-c)$$

$$\nabla \cdot \mathbf{u}_g = 0, \quad \bar{\rho} Re \left[\frac{\partial \mathbf{u}_g}{\partial t} + \mathbf{u}_g \cdot \nabla \mathbf{u}_g \right] = \nabla \cdot \mathbf{P}_g; \quad \mathbf{P}_g = -p_g \mathbf{I} + \bar{\mu} [\nabla \mathbf{u}_g + (\nabla \mathbf{u}_g)^T], \quad \mathbf{r} \in \Omega_g \quad (4.2a-c)$$

where \mathbf{P} , \mathbf{u} and p are the stress tensor, velocity and pressure in the fluid; \mathbf{I} is the metric tensor of the coordinate system. The non-dimensional parameters are the Reynolds number $Re = \rho \sigma R / \mu^2$ based on the liquid's properties, the gas-to-liquid density ratio $\bar{\rho} = \rho_g / \rho$ and the corresponding viscosity ratio $\bar{\mu} = \mu_g / \mu$.

Here, we have assumed that both the liquid and gas are incompressible which is valid if the Mach number $M = U/a$, where a is the speed of sound, in each fluid is small throughout the drops' motion. The fastest speed will be at the bridge front for the coalescence of the lowest-viscosity drops considered, and the largest Mach number will be in the air phase, where $a \sim 340 \text{ m s}^{-1}$ as opposed to the liquid where it is many times larger. A good estimate for the maximum speed U , as confirmed *a posteriori* by computations, is the capillary speed $U_v = \sigma / \mu$ which is a maximum of 20 m s^{-1} for the liquids considered giving in the air phase $M = 0.06$. Thus, our assumption of incompressibility is well justified, especially given that in the well-known isentropic formulas of gas dynamics the magnitude of the density variation is proportional to M^2 .

The conventional boundary conditions used for free-surface flows are the kinematic condition, stating that the fluid particles forming the free surface stay on the free surface at all time; the continuity of both components of velocity across the interface; and the balance of tangential and normal forces acting on an element of the free surface from the two bulk phases and from the neighbouring surface elements:

$$\frac{\partial f}{\partial t} + \mathbf{u} \cdot \nabla f = 0, \quad \mathbf{u}_g = \mathbf{u}, \quad (4.3a,b)$$

$$\mathbf{n} \cdot (\mathbf{P} - \mathbf{P}_g) \cdot (\mathbf{I} - \mathbf{n}\mathbf{n}) = \mathbf{0}, \quad \mathbf{n} \cdot (\mathbf{P} - \mathbf{P}_g) \cdot \mathbf{n} = \nabla \cdot \mathbf{n}. \quad (4.4a,b)$$

Here $f(r, z, t) = 0$ describes the *a priori* unknown free-surface shape, with the unit normal vector $\mathbf{n} = \nabla f / |\nabla f|$ pointing into the liquid, and the tensor $(\mathbf{I} - \mathbf{n}\mathbf{n})$ extracts the component of a vector parallel to the surface with the normal \mathbf{n} .

At the plane of symmetry $z=0$, the standard symmetry conditions of impermeability and zero tangential stress are applied

$$\mathbf{u} \cdot \mathbf{n}_s = 0, \quad \mathbf{n}_s \cdot \mathbf{P} \cdot (\mathbf{I} - \mathbf{n}_s \mathbf{n}_s) = \mathbf{0}, \quad \mathbf{r} \in \partial \Omega; \quad (4.5a,b)$$

$$\mathbf{u}_g \cdot \mathbf{n}_s = 0, \quad \mathbf{n}_s \cdot \mathbf{P}_g \cdot (\mathbf{I} - \mathbf{n}_s \mathbf{n}_s) = \mathbf{0}, \quad \mathbf{r} \in \partial \Omega_g, \quad (4.6a,b)$$

where \mathbf{n}_s is the unit normal to the plane of symmetry. In the conventional model we are studying here, the free surface is assumed to always be smooth so that where it meets the plane of symmetry we have $\mathbf{n} \cdot \mathbf{n}_s = 0$.

On the axis of symmetry $r = 0$, the standard normal and tangential velocity condition state that the velocity has only the component parallel to the axis and the radial derivative of this component is zero (the velocity field is smooth at the axis),

$$\mathbf{u} \cdot \mathbf{n}_a = 0, \quad \frac{\partial}{\partial r} [\mathbf{u} \cdot (\mathbf{I} - \mathbf{n}_a \mathbf{n}_a)] = 0, \quad r = 0; \quad (4.7a,b)$$

where \mathbf{n}_a is the unit normal to the axis of symmetry in the (r, z) -plane.

For the case of coalescing free spheres, the free surface is assumed smooth at the apex $r = 0, z = h(t)$ so that $\mathbf{n} \cdot \mathbf{n}_a = 0$ there, whilst the case of coalescing pinned hemispheres requires more conditions to account for the presence of the syringe. Specifically, at the point in the (r, z) -plane where the (initially hemispherical) free surface meets the syringe tip, we have a pinned contact line:

$$f(1, 1, t) = 0 \quad (t \geq 0). \quad (4.8)$$

It is assumed that in the far field, the exterior gas and the liquid inside the syringe are at rest, so that

$$\mathbf{u}, \mathbf{u}_g \rightarrow \mathbf{0} \quad \text{as } r^2 + z^2 \rightarrow \infty, \quad (4.9)$$

whilst on the cylinder's surface, no-slip is applied

$$\mathbf{u} = \mathbf{u}_g = \mathbf{0} \quad \text{at } r = 1, \quad z \geq 1. \quad (4.10)$$

The conventional model postulates that, once the drops come into contact, they produce a smooth free surface, i.e. they coalesce on the sub-fluid-mechanical scale and round the corner enforced by the drops' configuration at the moment of touching. A bridge of zero radius with infinite azimuthal and longitudinal curvatures of the free surface is obviously a singular configuration and hence cannot be used as a starting point for computation; one has to use an approximation to this configuration, i.e. specify the initial shape as having, near the origin, a tiny but finite-size bridge with some radius $r_{\min} > 0$, where the free surface crosses the plane of symmetry at a right angle. By introducing explicitly the radius r_{\min} from which our computations start, we ensure that they are mesh-independent under refinement, unlike those studies in which the initial bridge radius was defined in terms of the mesh, e.g. Menchaca-Rocha *et al.* (2001). Then, we can study the effect of a finite r_{\min} separately.

The free-surface shape far away from the origin (i.e. from the point of the initial contact) is initially the undisturbed hemispherical/spherical drop. A shape which satisfies these criteria can be taken from Hopper (1984), i.e. the analytic two-dimensional solution to the problem for Stokes flow. In parametric form, the initial free-surface shape is taken to be

$$r(\theta) = \sqrt{2}[(1 - m^2)(1 + m^2)^{-1/2}(1 + 2m \cos(2\theta) + m^2)^{-1}](1 + m) \cos \theta, \quad (4.11)$$

$$z(\theta) = \sqrt{2}[(1 - m^2)(1 + m^2)^{-1/2}(1 + 2m \cos(2\theta) + m^2)^{-1}](1 - m) \sin \theta, \quad (4.12)$$

for $0 < \theta < \theta_u$, where m is chosen such that $r(0) = r_{\min}$ is the initial bridge radius, which we choose, and θ_u is chosen such that $r(\theta_u) = z(\theta_u) = 1$ for hemispherical drops and $r(\theta_u) = 0$ for spherical ones. Notably, for $r_{\min} \rightarrow 0$ we have $m \rightarrow 1$ and

$r^2 + (z - 1)^2 = 1$, i.e. the drop's profile is a semicircle of unit radius which touches the plane of symmetry at the origin as required.

An alternative approach, considered briefly in § 6.1, is to start the simulation with a truncated sphere of radius r_{min} which meets the plane-of-symmetry at an angle $\theta = 180^\circ$ and then to rapidly change θ until a smooth free surface ($\theta = 90^\circ$) is obtained. To do so, one can prescribe the angle $\theta(t) = 180^\circ - 90^\circ \min(1, t/T_r)$ where T_r is the timescale over which the free surface is 'rounded'.

Finally, we need to prescribe the fluid initial velocities in the two phases, which we will assume to be zero:

$$\mathbf{u} = \mathbf{u}_g = \mathbf{0} \quad \text{at } t = 0. \quad (4.13)$$

This condition is based on the assumption that the drops are brought together slowly. Computations confirm that if instead the maximum possible approach velocity $8 \times 10^{-5} \text{ m s}^{-1}$ from the experiments in Paulsen *et al.* (2011) is used to formulate an initial condition, then the results obtained are graphically indistinguishable from those presented. This is to be expected as the initial bridge speeds are many times larger than the approach speeds used.

5. Computational approach

In order to tackle the coalescence phenomenon in its entirety, we must solve a two-phase free-boundary problem with effects of viscosity, inertia and capillarity all present, so that a computational approach is unavoidable. To do so, we use a finite-element framework which was originally developed for dynamic wetting flows and has been thoroughly tested in Sprittles & Shikhmurzaev (2012c, 2013) as well as being applied to flows undergoing high free-surface deformation in Sprittles & Shikhmurzaev (2012b), namely microdrop impact onto and spreading over a solid surface. Notably, the method has been specifically designed for multiscale flows, so that the very small length scales associated with the early stages of coalescence can be captured alongside the global dynamics of the two drops' behaviour. In other words, all of the spatiotemporal scales which are resolved in the electrical experiments mentioned earlier (Paulsen *et al.* 2011), as well as the scales associated with later stages of the drop's evolution, which are accessible to optical observation, can, for the first time, be resolved simultaneously. A user-friendly step-by-step guide to the implementation of the method has already been provided (Sprittles & Shikhmurzaev 2012c, 2013) and, although this is for a single-phase flow, the extension to a two-phase flow is a relatively straightforward procedure which does not introduce any conceptually new ideas to the framework already used. This code has also been benchmarked in Sprittles & Shikhmurzaev (2012a) against previous simulations of coalescence in Paulsen *et al.* (2012) at the scales resolved in that work.

The computational domain is truncated, so that 'far-field' conditions on the gas and the liquid in the cylinder must be applied at a finite distance from the origin. To do so, we apply 'soft' conditions on these boundaries and ensure that these boundaries are sufficiently far from the coalescing hemispheres that neither the conditions specified there nor any further increase of r_{far} and z_{far} (figure 2) have any influence on the drops' dynamics.

6. Parametric study

A systematic study of the governing parameters in the coalescence process will now be considered and then, in § 7, the results will be compared with the available

experimental data. An advantage of this approach is that the parameters can be independently varied in the computations whereas in the experiments often it is the viscosity which is varied, so that Re and $\bar{\mu}$ are related, which makes isolating the effect of each parameter more difficult. Our approach here will be to consider the simplest possible set-up first, and then add layers of complexity. For example, first of all a passive gas will be considered ($\bar{\mu} = \bar{\rho} = 0$), and only once the role of the remaining parameters has been established will the gas dynamics be considered. Once the full parametric study and comparison with experiment have been performed, this will all be tied together with the published literature in § 8.

To understand the different regimes of drop coalescence, the appropriate scalings in these regimes, the crossover between them and their comparison to experiments which are able to capture many decades of bridge radius, results will be given on log–log plots.

6.1. Influence of initial conditions, dimensionality and geometry

To estimate the influence of the initial conditions compared with the solution obtained as the initial bridge radius $r_{min} \rightarrow 0$, computations for finite r_{min} are compared with Hopper's solution (2.1) which was obtained for the inertialess coalescence of two-dimensional liquid cylinders. The possible effect of errors associated with a finite initial radius is particularly important when considering the initial stages of motion where small changes in the initial time can sometimes drastically alter the agreement between experiments and scalings, see Thoroddsen *et al.* (2005, § 5.3). To be consistent with Hopper's solution, we will take $Re = 0$ and consider the gas to be passive.

6.1.1. Effect of finite minimum radius

Simulations shown in figure 3, performed for $r_{min} = 10^{-4}$, show that the computed solution (curve 3) for the bridge radius of free cylinders coalescing is graphically indistinguishable from Hopper's exact solution (dashed line) from $r = 10^{-3}$ (marked by the lower horizontal dash-dot line) onwards. This is despite the fact that in Hopper's solution at $t = 0$ the bridge radius is infinitesimal whereas in the computations $r = 10^{-4}$. As a consequence of the observed agreement from $r = 10^{-3}$, we do not have to concern ourselves with calculating the time t_0 at which the bridge would reach a radius r_{min} , and then subtract this from the time elapsed in the computation t , i.e. to plot r against $t - t_0$; instead, we can simply plot computations from $r = 10^{-3}$ knowing that the error associated with starting at a finite bridge radius is negligible.

6.1.2. Equivalence of two-dimensional and three-dimensional solutions

Although Hopper's solution is strictly valid only for two-dimensional motion, results in Eggers *et al.* (1999) and Paulsen *et al.* (2012) suggest that this expression may also approximate the initial stages of the axisymmetric three-dimensional solution as well. The curves in figure 3 confirm that this is the case: curves 1 and 3 obtained for coalescing spheres and cylinders, respectively, are graphically indistinguishable up to at least $r = 10^{-1}$ (upper horizontal dash-dot line). Clearly, at longer times the two curves must diverge as the two configurations have different equilibrium bridge radii r_{eqm} , with $r_{eqm} = 2^{1/2} = 1.41$ for cylinders and $r_{eqm} = 2^{1/3} = 1.26$ for spheres.

To re-enforce our arguments about the effect of the initial bridge radius, computations for free spheres with a larger $r_{min} = 10^{-3}$ are shown by curve 2 in figure 3 and it can be seen that in this case after $r = 10^{-2}$ the curve falls on top of the computed

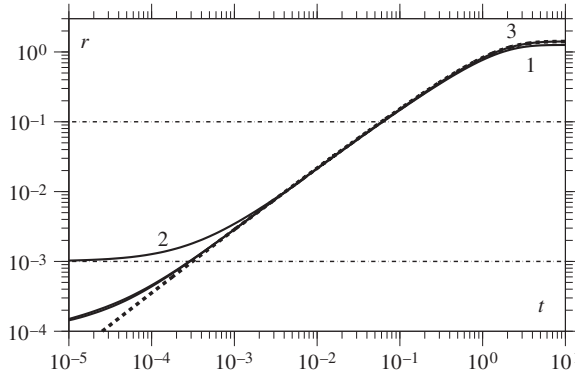


FIGURE 3. Bridge radius as a function of time for the case $Re = 0$ compared with Hopper's solution (2.1), the dashed line. Curve 1 is for three-dimensional free spheres with $r_{min} = 10^{-4}$, curve 2 the same except that $r_{min} = 10^{-3}$ and curve 3 is for two-dimensional free cylinders ($r_{min} = 10^{-4}$).

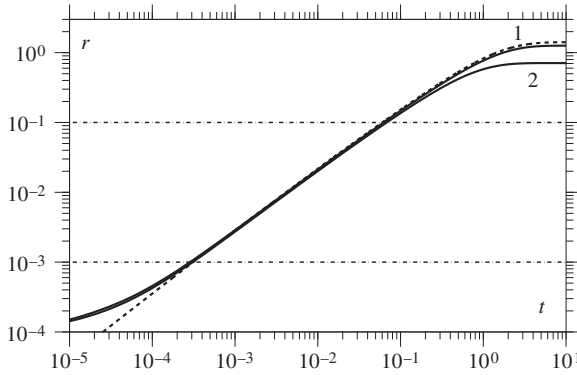


FIGURE 4. Bridge radius as a function of time for the case $Re = 0$ for free spheres (curve 1) and pinned hemispheres (curve 2). The dashed lined is Hopper's solution (2.1).

solution for $r_{min} = 10^{-4}$ (curve 1) and hence also Hopper's solution. Thus, for both r_{min} considered, at $r = 10r_{min}$ the curves are insensitive to the finite initial radius used. Notably, computations confirm that for the range of Re considered in this work, similar levels of insensitivity to the initial finite radius were observed.

6.1.3. Effect of geometry

In figure 4, the evolution of the bridge radius for the coalescence of three-dimensional free spheres (curve 1) and pinned hemispheres (curve 2) is shown. Very slight deviations between the two curves are observed for the entire time; however, until $r = 10^{-1}$ these differences are so small that they are likely to fall below the resolution of any experimental accuracy. Therefore, the effect of geometry can be considered negligible until $r = 10^{-1}$ after which the bridge of pinned hemispheres is slower as it asymptotes to a smaller equilibrium radius of $r_{eqm} = 0.71$ than the free spheres ($r_{eqm} = 1.26$).

Notably, the case $Re = 0$ is most likely to highlight any effect of the global geometry (far away from the bridge) on the initial stages of the bridge's evolution as

at finite Reynolds number, as we will see later, the flow near the bridge will be more ‘localised’ in comparison with Stokes flow, where the entire body of fluid moves from $t = 0$.

6.1.4. Effect of initial free surface shape

To further re-enforce the point, that the effect of our initial conditions is negligible from $r = 10^{-3}$, we have compared the two different start-up strategies proposed in §4, namely to either (a) use Hopper’s solution as an initial condition for the free surface shape or (b) use a truncated sphere and make the free surface smooth where it meets the plane of symmetry over a timescale T_r , which we choose here to be $T_r = 10^{-5}$. Again, from $r = 10^{-3}$, the curves obtained from either start-up strategy were seen to be graphically indistinguishable.

6.1.5. Summary

For $r_{min} = 10^{-4}$, from $10^{-3} < r < 10^{-1}$, i.e. what will be considered as the ‘initial stages of motion’, the bridge evolution of the coalescing drops is graphically indistinguishable:

- (i) from those obtained for $r_{min} = 0$;
- (ii) for spheres and cylinders of the same radius;
- (iii) for free spheres and pinned hemispheres.

6.2. Effect of the Reynolds number

If the parameters governing the initial configuration are fixed, and the gas is still passive, then the only parameter remaining is the Reynolds number Re . Unless specified, computations are with pinned hemispheres, which in all cases considered give the same behaviour as free spheres up to at least $r = 0.1$.

6.2.1. Small Reynolds numbers: $Re \leq 1$

All curves for $Re \leq 1$ are seen to be graphically indistinguishable on a log–log plot from those obtained for $Re = 0$ in figure 5. This is an intriguing result: measurements of the bridge radius show no evidence of an ILV regime for $Re \leq 1$.

As can be seen from curve 2 in figure 6, for $Re \leq 1$ it is Hopper’s exact solution (2.1) that provides the best approximation of the computed bridge front evolution for $r < 0.1$, confirming again that this range is described by inertialess Stokes flow. In other words, we are in what has classically been referred to as a ‘viscous regime’. Curve 3 is the expression (2.3) from Eggers *et al.* (1999), which is an asymptotic approximation of Hopper’s solution (curve 2). It is seen to be inaccurate in the range $10^{-3} < r < 10^{-1}$ of interest, as suggested in Eggers *et al.* (1999) where $r < 0.03$ is said to be the range of applicability of their formula. In a previous work (Sprittles & Shikhmurzaev 2012a), this expression was shown to describe reasonably the conventional model when $C_v = C_v(Re)$ in (2.3) was fitted, which, strictly speaking, it should not be, as (2.3) was originally derived as an approximation to the exact expression (2.1). Notably, the linear expression (curve 1), indicative of the ILV regime, is also seen to diverge from the computed result (curve 0).

6.2.2. Large Reynolds numbers: $Re \geq 1$

From figure 5, it can be seen that curve 1, for $Re = 10$, has diverged noticeably from the Stokes flow solution (curve 0) by around $r = 0.1$. A further increase in the

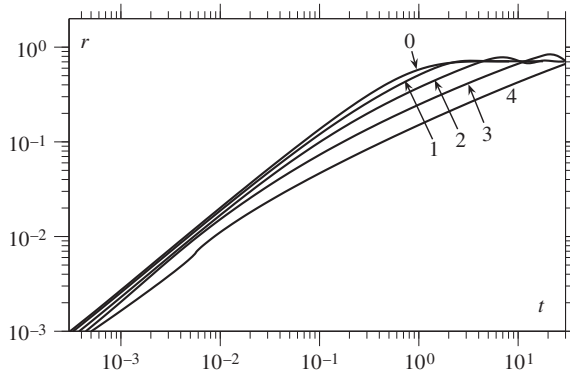


FIGURE 5. Bridge radius as a function of time for a variety of different Reynolds numbers. Curve 0 is for $Re = 0$ (curves for $Re \leq 1$ are graphically indistinguishable from it); 1, $Re = 10^1$; 2, $Re = 10^2$; 3, $Re = 10^3$; and 4, $Re = 10^4$.

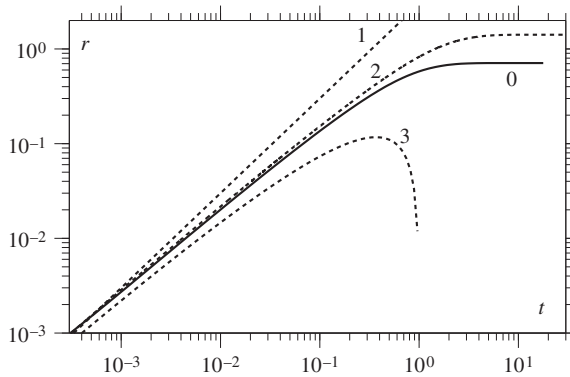


FIGURE 6. Comparison of the full numerical solution for $Re = 0$ (and hence all $Re \leq 1$) curve 0 with scalings and the exact solution for free cylinders. Curve 1, linear plot (2.5) of $r = 3t$; curve 2, Hopper's solution for free cylinders (2.1); curve 3, formula (2.3) for a passive gas, i.e. $r = -(1/\pi)t \ln t$. It is clear that Hopper's solution best approximates the full numerical solution.

Reynolds number to $Re = 100$ (curve 2) ensures no agreement with the Stokes solution, although the divergence is rather small for $r < 0.01$. Clearly, once $Re \geq 10^3$ significant deviations from the Stokes flow solution are seen, so that inertial effects are becoming increasingly important.

Given that the inertial regime is characterised by a different timescale $T_i = (\rho R^3/\sigma)^{1/2}$ as opposed to $T_v = \mu R/\sigma$, in figure 7 we plot the curves of figure 5 against the (dimensionless) inertial time $t_i = t(T_v/T_i) = t/Re^{1/2}$ instead of the viscous one.

The 'inertial regime' itself is usually characterised by the scaling in (2.4), and by fitting the prefactor ($C_i = 1.5$) to the curve from the highest Reynolds number considered (curve 4), we obtain the dashed line A2 in figure 7. One can see that at $Re = 10^4$ (curve 4), the inertial scaling (curve A2) approaches the full numerical solution at around $r = 10^{-2}$, which is consistent with the inertial regime being entered when $r \sim Re^{-1/2}$. For the case of $Re = 10^3$ (curve 3), fitting (2.5) to the early time

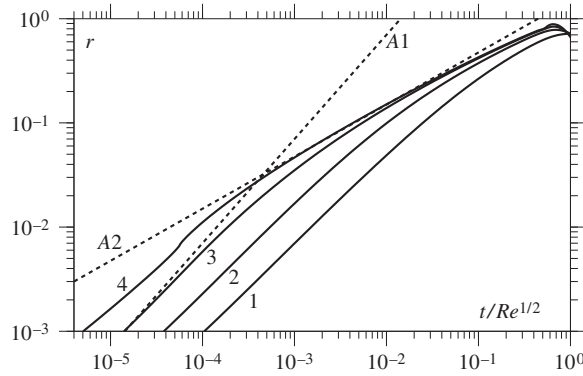


FIGURE 7. Curves from figure 5 plotted against the time scaled using T_i , i.e. r against $t_i = t/Re^{1/2}$, characteristic of the inertia-dominated regime as opposed to T_v in figure 5. Curve 1, $Re = 10^1$; curve 2, $Re = 10^2$; curve 3, $Re = 10^3$; and curve 4, $Re = 10^4$. The dashed line A1 is for (2.5), i.e. a linear curve ($r = 70t_i$) and A2 is for (2.4), i.e. the scaling $r = 1.5t_i^{1/2} = 1.5t^{1/2}/Re^{1/4}$.

behaviour gives dashed line A1, so that if the crossover is defined where curve A2 meets curve A1, as considered in Paulsen *et al.* (2011), this will occur at around $r \sim 2 \times 10^{-2}$, i.e. again at $r \sim Re^{-1/2} = 10^{-3/2} = 3 \times 10^{-2}$. The details of this crossover will be considered in far greater details in § 7.1.

Notably, the scaling (2.4) has a rather limited region of applicability, even when Re is sufficiently large to ensure the drops are in an ‘inertial regime’. This aspect is considered in detail in Sprittles & Shikhmurzaev (2014b), where an improved scaling law for this regime is derived and shown to agree well with both the fully computed solution as well as a range of experimental data from the published literature.

For $Re = 10^2$ (curve 2) and $Re = 10^1$ (curve 1), both (2.1) and (2.4) fail to approximate any of the observed behaviour, meaning that this is a region of parameter space where both the viscous and inertial forces are important, so that simplified expressions based on neglecting either of these will be inherently inaccurate. This area of parameter space will later be referred to as the ‘transition’ region and will be rigorously defined in § 8.

6.2.3. Global motion and the ILV regime

It has been shown that for $Re \leq 1$, the early stage of the bridge’s propagation is well approximated by Hopper’s solution (2.1) for free cylinders whilst for $Re > 1$ all of the proposed expressions fail to describe the initial stages of motion. At first sight, this appears to contradict the results of Paulsen *et al.* (2012), where it was shown that for $Re \leq 1$ ($Oh > 1$), an ILV regime is present where inertia cannot be neglected, so that (2.1) does not hold. Simulations and experiments on free spheres confirmed, by measuring the speed at which the centres of the drops move towards each other, that the Stokes flow solution does not accurately describe the global motion of the drops in the very initial stages of motion.

In figure 8, we plot the results of simulations performed using free spheres, showing the distance which the apex height h of the drop (figure 2) has moved from its initial position $h_0 = 2$ as a function of bridge’s radius. This is a measure indicative of the influence of the coalescence dynamics on the three-dimensional global motion and thus Hopper’s two-dimensional solution cannot provide an approximate expression for

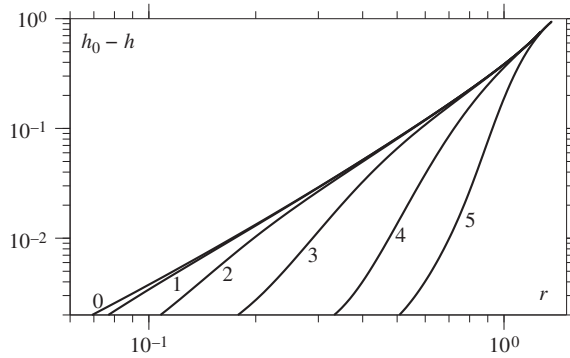


FIGURE 8. Distance $h_0 - h$ that the apex has moved plotted against bridge radius r for different Reynolds numbers: curve 0, $Re = 0$; curve 1, $Re = 10^{-3}$; curve 2, $Re = 10^{-2}$; curve 3, $Re = 10^{-1}$; curve 4, $Re = 1$; and curve 5, $Re = 10$.

the evolution of h . From figure 8, we can see that even at very small Reynolds number, the curves do not immediately fall onto the computed Stokes flow solution (curve 0), as could have been anticipated from the results in Paulsen *et al.* (2012). For example, at $Re = 10^{-3}$ (curve 1), the bridge travels as far as $r = 0.1$ before it approaches the Stokes flow solution. For $Re = 10^{-2}$ (curve 2), it is $r = 0.2$ and for $Re = 10^{-1}$ (curve 3) it takes until $r = 0.6$. At higher Reynolds number, the Stokes flow solution is not approached until the drop starts to reach its equilibrium state.

Thus, as first observed in Paulsen *et al.* (2012), for $0 < Re \leq 1$ it takes a certain time until the global motion of the drops is approximately described by the Stokes flow solution. However, during this period, the bridge radius is described perfectly by the Stokes flow solution. Therefore, we find that the ILV regime is a description of the global motion of the drops, as opposed to being an expression for the local bridge front evolution, as originally suggested. This means that there is a boundary layer around the bridge front region, which grows in time and inside which the flow is inertialess. Outside this region it is the inertial effects that are important, so that the bridge evolution can be described by Stokes flow solution whilst the global motion of the drops takes some time to follow this behaviour.

6.2.4. Summary

It has been shown that in the initial stages of coalescence ($10^{-3} < r < 10^{-1}$) described in the framework of the conventional model, for $Re \leq 1$:

- (i) the bridge propagation is accurately described by (2.1), i.e. by Hopper's exact solution obtained in the framework of the Stokes flow theory; neither (2.3) nor (2.4) are accurate;
- (ii) the ILV regime describes the global motion and can be observed by monitoring the motion of the apex of free spheres.

For $Re > 1$:

- (i) for $Re \leq 10^2$ a truly inertial regime, with C_i in (2.4) fixed, is never reached;
- (ii) for $Re \geq 10^3$ an inertial regime is entered when $r \sim Re^{-1/2}$ after which $r \simeq 1.5t_i^{1/2}$;

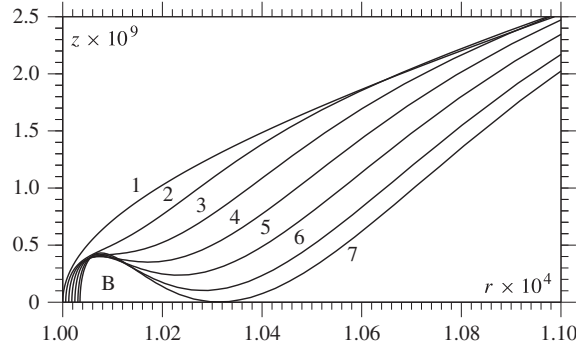


FIGURE 9. Free surface profiles for the case of two low-viscosity liquid drops ($Re = 10^4$) coalescing in a passive gas, calculated in the framework of the conventional model, showing the formation of a toroidal bubble (recalling that $z=0$ is a plane of symmetry) at location 'B'. Curves 1–6 are in equal time steps from $t=0$ through to $t=10^{-7}$ with curve 7, at the time when the free surface touches the plane of symmetry ($z=0$), at $t=1.14 \times 10^{-7}$. This bubble does not form if the dynamics of the viscous ambient gas is accounted for.

6.3. The influence of a viscous gas

Having established the role of the parameters for coalescence in a passive gas, we now consider how a dynamically active viscous gas will effect the process. To estimate reasonable parameter values, consider typical liquids with viscosities $\mu \sim 10^{-3}$ – 10 Pa s and densities $\rho \sim 10^3$ kg m $^{-3}$, in contact with gases at atmospheric pressure having $\mu_g \sim 10$ μ Pa s and $\rho_g \sim 1$ kg m $^{-3}$. Then $\bar{\mu} \sim 10^{-6}$ – 10^{-2} and $\bar{\rho} \sim 10^{-3}$.

6.3.1. Toroidal bubbles: suppression of their formation by a viscous gas

Before examining the quantitative effect which a viscous gas has on the propagation of the bridge front, we will look at the qualitative behaviour of the system in the early stages of coalescence of low-viscosity drops, where toroidal bubbles have been obtained in local inviscid boundary-integral calculations (Oguz & Prosperetti 1989; Duchemin *et al.* 2003). A trail of toroidal bubbles are formed at high Re when capillary waves generated by the disturbance to the free-surface shape caused by the bridge propagation have a large enough amplitude to reconnect in front of the bridge (figure 9). Notably, although the bubble formed in figure 9 for $Re = 10^4$, located at 'B', has microscopic dimensions for typical drop sizes, this bubble, should it appear, is likely to be the first in a trail of bubbles of increasing size, as shown in Duchemin *et al.* (2003), so that the question as to whether or not this initial bubble forms is indicative of whether or not macroscopic bubbles could be generated and experimentally detected. In fact, the end of the toroidal bubble formation stage is indicated by a slight 'kink' in curve 4 of figure 5 (at $r, t \sim 10^{-2}$), which disappears when the gas' viscosity is accounted for (cf. curve 3 in figure 12). As explained in Sprittles & Shikhmurzaev (2012a), current computational approaches do not accurately capture toroidal bubble formation, but since these bubbles, as shown below, are unphysical, there is little motivation to develop the advanced techniques required to do so.

As the predicted toroidal bubbles have never been observed experimentally, it is of particular interest to see whether the presence of a viscous gas is able to suppress

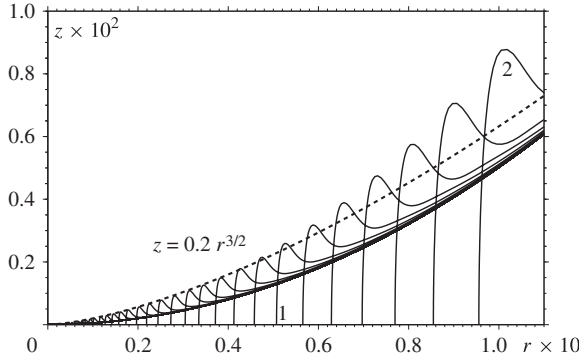


FIGURE 10. Free surface profiles for the case of two low-viscosity liquid drops ($Re = 10^4$) coalescing in a viscous gas with $\bar{\mu} = 6 \times 10^{-3}$ calculated in the framework of the conventional model. The dashed line shows the scaling for the height (i.e. distance from the plane of symmetry) of the gas bubble predicted in Eggers *et al.* (1999) as a function of bridge front radius. Note that the scales in the r and the z directions are different, so that the cross-section of the trapped air bubble in front of the bridge is actually more circular than it appears here. The profiles correspond to different times from the onset of coalescence; curve 1 corresponds to $t = 2.3 \times 10^{-2}$ and curve 2 corresponds to $t = 3.5 \times 10^{-2}$, with equal time spacing in between and outside.

their formation. This cannot be inferred from previous works which consider either no inertial effects, so that there is no mechanism for bubble formation (Eggers *et al.* 1999); no viscous effects, so that bubble formation cannot be suppressed by the gas (Duchemin *et al.* 2003); or no gas dynamics at all, as in previous computational works (Paulsen *et al.* 2012; Sprittles & Shikhmurzaev 2012a).

In figure 10, we show the results of calculations for the coalescence of low-viscosity drops (also $Re = 10^4$) in air ($\bar{\mu} = 6 \times 10^{-3}$). As one can clearly see, a viscous gas acts as a barrier to toroidal bubble formation, which results in an entirely different behaviour of the free surface from that previously observed for a passive gas, i.e. physically a vacuum, where toroidal bubbles are formed (figure 9). It can be seen that the propagating bridge creates a capillary wave and pushes a gradually growing pocket of air in front of itself, and it is the dynamics of this pocket of air that now prevents the free surface of each of the drops from reaching the plane of symmetry, reconnecting, and trapping a toroidal bubble of air.

As can be seen, the computed free-surface shape is consistent with the predictions in Eggers *et al.* (1999) that the radius of the curvature at the bridge front scales like $r^{3/2}$, in contrast to the case of coalescence in a passive gas, where the radius of curvature scales like r^3 . Notably, for the case of a viscous gas, the radius of curvature at the bridge front is larger than the undisturbed free-surface height, which scales like r^2 , so that the gas bubble protrudes ‘into’ the liquid drop and causes a local maximum in the free-surface height $z = z(r)$. As shown in figure 10 by the dashed line, the latter scales as $r^{3/2}$ for a considerable distance.

Notably, for realistic parameters it is the viscosity of the ambient gas that plays the key role in the suppression of the toroidal bubble appearance. This is highlighted by the fact that, if we set $\bar{\rho} = 0$, toroidal bubbles are not formed until the gas-to-liquid viscosity ratio is reduced to $\bar{\mu} \approx 10^{-7}$. Therefore, in reality it is always the viscosity and not the density of the ambient gas that holds the key to the toroidal

bubble suppression. Indeed, under normal conditions, the viscosity of the gas is above a certain value, say, $1 \mu\text{Pa s}$, so that for the gas-to-liquid viscosity ratio to be of the order of 10^{-7} , one must have a liquid with viscosity of the order of 10 Pa s , and, as shown in Sprittles & Shikhmurzaev (2012a), even for coalescing drops of much lower viscosity than 10 Pa s , the toroidal bubble does not form even if the ambient fluid is a vacuum. The same point can be made in another way: if we take two drops of a low-viscosity liquid that would produce a toroidal bubble in a vacuum and replace the vacuum with a gas of gradually increasing viscosity and density, the gas' viscosity would prevent the bubble formation long before the gas-to-liquid density ratio has a noticeable effect on the process.

Having established that the presence of a viscous gas completely alters the initial stages of the coalescence process for a low-viscosity liquid, it is of interest to study how the parameters associated with the gas, namely the density and viscosity ratios, affect the motion.

6.3.2. Influence of gas density

For $\bar{\rho} \leq 0.01$, which covers the range of realistic liquid-gas systems, the influence of the finite gas density on the dynamics of coalescence are seen to be negligible. Once $\bar{\rho} = 0.1$ an effect on the bridge front evolution for small radii can be observed, but this only becomes relevant for liquid-liquid systems, which are not considered here in any detail. Therefore, henceforth the effect of this parameter will not be considered.

6.3.3. Influence of gas viscosity

Consider now how the viscosity ratio $\bar{\mu}$ affects the coalescence event. First, taking $Re = 10^2$ as a representative case, we show in figure 11 that the viscosity of the gas does have an influence on the initial stages of coalescence and that, as one would hope, for very small viscosity ratio, e.g. for $\bar{\mu} = 10^{-6}$ (curve 2), the result is almost indistinguishable from the case of a passive gas examined in § 6.2 (curve 1). At the highest viscosity ratio considered $\bar{\mu} = 1$ (curve 5), the effect is rather substantial, with a noticeable difference from the passive gas situation (curve 1) well past $r = 0.1$. The viscosity ratio of $\bar{\mu} = 1$ is, of course, unrealistic for liquid-gas systems, but it is entirely relevant to liquid-liquid ones to which our analysis fully applies. This reduction in the speed of propagation of the bridge's front is due to the additional energy dissipated in the squeezing of fluid out of the thin gap formed ahead of the bridge (figure 10).

Figure 12 shows how the inclusion of a gas ($\bar{\mu} = 10^{-2}$) affects the coalescence process at different Reynolds numbers (in the liquid, as the inertial effects in the gas have a negligible influence). In all cases, the gas has a noticeable effect on the motion compared with the passive gas cases (dashed lines) but what is particularly interesting is that for all Re considered, the curve from the viscous-gas case converges to the passive-gas one at around $t = 1$, i.e. dimensionally at the viscous timescale $T_v = \mu R / \sigma$. However, at this time ($t = 1$), the bridge radii depends on Re , with a smaller the Reynolds number (curve 1 is for $Re = 0$) giving a larger bridge radius. In other words, we observe that for a fixed viscosity ratio, the lower the Reynolds number is in the liquid, the more of the coalescence process is affected by the presence of the gas. This will help to explain our findings in § 7 where the effects of Re and $\bar{\mu}$ can no longer be varied independently.

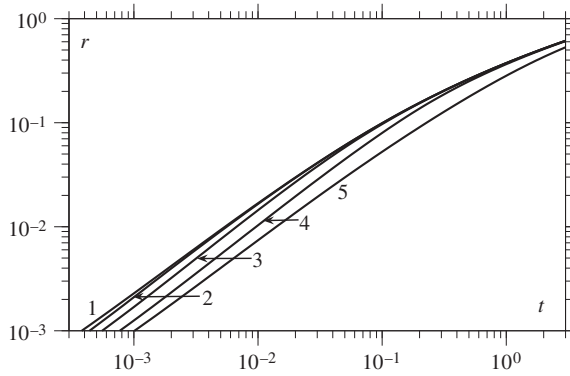


FIGURE 11. Influence of gas viscosity on the time-dependence of the radius of the bridge connecting the coalescing drops calculated for fixed $Re = 10^2$ with: curve 1, $\bar{\mu} = 0$; curve 2, $\bar{\mu} = 10^{-6}$; curve 3, $\bar{\mu} = 10^{-4}$; curve 4, $\bar{\mu} = 10^{-2}$; and curve 5, $\bar{\mu} = 1$.

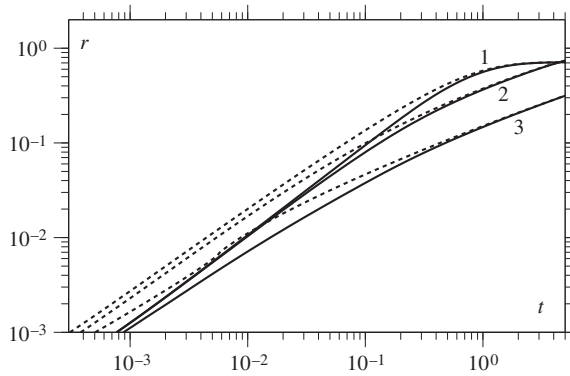


FIGURE 12. The effect of the Reynolds number on the time-dependence of the radius of the bridge connecting the coalescing drops calculated for a fixed viscosity ratio $\bar{\mu} = 10^{-2}$ (solid lines) compared with the $\bar{\mu} = 0$ case (dashed lines) with: curve 1, $Re = 0$; curve 2, $Re = 10^2$; and curve 3, $Re = 10^4$.

6.3.4. Scaling laws to account for the gas' influence

In § 6.2 it has been shown for the passive gas case that, for $Re = \bar{\mu} = 0$, (2.1) accurately approximates the initial stages of motion whilst (2.3) is less useful. However, whilst (2.1) is exclusively for one-phase motion without any indication of what effect the dynamics of an ambient gas may have on the initial stages, the scaling law (2.3) predicts that taking into consideration the viscosity of the gas will slow the initial stages of coalescence by a factor of four, and, notably, this change in behaviour is predicted to be independent of the viscosity ratio for $r < \bar{\mu}^{2/3}$.

From figure 13, where the effect of switching from an inviscid exterior (curve 1) to viscous one (curves 2 and 3) at $Re = 0$ is considered, we can immediately see that (2.3) is both qualitatively and quantitatively incorrect: the initial stages depend strongly on the viscosity ratio with a larger $\bar{\mu}$ resulting in a slower coalescence. In particular, curve 3, for $\bar{\mu} = 1$, is always well below curve 2, obtained for $\bar{\mu} = 10^{-4}$.

In an attempt to quantify the effect of the viscosity ratio, the dashed lines in figure 13 are (2.1a,b) with fitted prefactors, i.e. instead of computing $r = f(t)$ given exactly by (2.1), we consider $r = Hf(t)$, where H is a constant chosen to produce

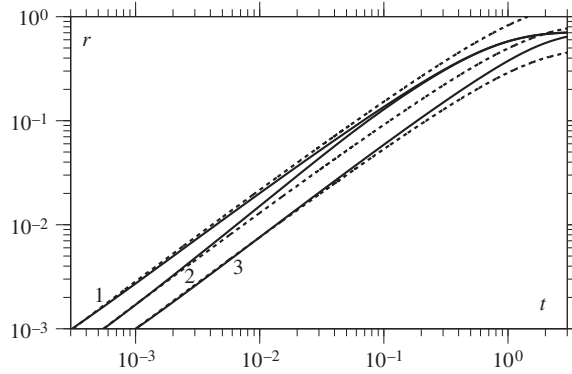


FIGURE 13. An illustration of the influence of the gas viscosity on the coalescence of drops (with $Re=0$): curve 1, $\bar{\mu}=0$; curve 2, $\bar{\mu}=10^{-4}$; and curve 3, $\bar{\mu}=1$. The top dashed line corresponds to (2.1) whilst the middle and lower lines are the same expression with a fitted prefactor of 0.6 and 0.35, respectively.

a best fit. It is found that for $\bar{\mu} = 0, 10^{-4}, 1$ these prefactors are, respectively, $H = 1, 0.6, 0.35$. This approach does not originate from any theory, but is simply intended to estimate the effect which a viscous gas has on the motion. It shows, in particular, that for a small viscosity ratio $\bar{\mu} = 10^{-4}$, the initial bridge speed is still decreased significantly, but that this effect does not last long, whilst for matched viscosities $\bar{\mu} = 1$ the bridge speed is decreased by roughly a factor of three for almost all of the initial stage of coalescence ($r < 0.1$). Notably, the different deviations of the dashed lines from the computed solutions suggest that any attempt to somehow make minor adjustments to the passive gas case to account for a viscous exterior are unlikely to work.

6.3.5. Summary

The following has been observed for liquid drops coalescing in the viscous gas usually considered in experiments, e.g. air at atmospheric pressure, for $Re \in (0, 10^4)$:

- (i) inertial effects in the gas have a negligible effect;
- (ii) the viscosity of the gas prevents toroidal bubble formation;
- (iii) the bridge evolution can be substantially slower in its initial stages, an effect which increases with the gas-to-liquid viscosity ratio $\bar{\mu}$;
- (iv) for fixed $\bar{\mu}$, lower Re results in the coalescence process being affected on a larger length scale;
- (v) Equation (2.3) does not capture the aforementioned effects.

7. Comparison with experiments

Having performed a systematic study of the conventional model's predictions, we now proceed to compare these to experimental data where parameters can no longer be independently varied. In particular, in the experiments of Paulsen *et al.* (2011), the liquids are water-glycerol mixtures, whose viscosity varies in the range of $\mu = 2\text{--}230$ mPa s, whilst the density ($\rho = 1200$ kg m $^{-3}$) and surface tension with air ($\sigma = 65$ mN m $^{-1}$) remain approximately the same. These experiments were conducted in air of density $\rho_g = 1.2$ kg m $^{-3}$ and viscosity $\mu_g = 18$ μ Pa s. Therefore, as the viscosity is varied, the Reynolds number and viscosity ratio are no longer

independent, and we have $\bar{\mu} = 4.6 \times 10^{-5} Re^{1/2}$. Using these material parameters, we arrive at

$$Re \in (1, 10^5), \quad \bar{\mu} = 4.6 \times 10^{-5} Re^{1/2} \in (10^{-4}, 10^{-2}), \quad \bar{\rho} = 10^{-3}. \quad (7.1a,b,c)$$

Notably, the range in (7.1) has already been covered in the parametric study of § 6, so that all that remains to be done is to compare the predictions of the conventional model with experimental data.

7.1. Collapse of data onto a ‘master curve’

In Paulsen *et al.* (2011), it is shown that data for the initial stages of bridge front evolution, collected from electrical measurements of the coalescence event over a range of different viscosity liquid, can be collapsed onto a master curve:

$$r/r_c = \frac{2}{1/(t/t_c) + 1/\sqrt{t/t_c}} \quad (7.2)$$

where t_c , r_c are referred to as the (dimensionless here) ‘crossover’ time and radius, where the dominant term in (7.2) changes. In particular, for $t \ll t_c$, there is linear growth $r/r_c \sim 2t/t_c$, and for later times, $t \gg t_c$, the scaling is of square-root type $r/r_c \sim 2\sqrt{t/t_c}$. Fitting r_c and t_c for every curve enables the dependence of the crossover time on Re to be established.

It is of interest to see whether a similar fit can be performed with the theoretical curves obtained from the conventional model. In figure 14, curves 1–5 for $Re = 10$ – 10^5 are fitted with the master curve by choosing (t_c, r_c) such that (7.2) goes through the computed curves at $r = 10^{-3}$ and $r = 10^{-1}$. The fit is relatively good, and the parameters used are plotted in figure 14 as a function of Reynolds number. Notably, as seen in the experiments (Paulsen *et al.* 2011), crossover time and radius scale with $Re^{-1/2}$ as opposed to with Re^{-1} , as suggested in some previous works, e.g. Eggers *et al.* (1999), Wu, Cubaud & Ho (2004) and Aarts *et al.* (2005). What this essentially means is that the characteristic length scale L appearing in the Reynolds number that determines the crossover value Re_c should be the (dimensional) bridge height $L \sim r_{dim}^2/R$ so that the crossover occurs when $Re_c = \rho \sigma r_{dim}^2/(\mu^2 R) \sim 1$, i.e. when $r \sim Re^{-1/2}$.

7.2. Direct comparison with experimental data

The analysis in § 7.1 suggests that many of the trends observed in the experiment are also seen from the computations using the conventional model. Here, a more direct comparison between theory and experiment, going further than simply confirming the correct scaling behaviour, is performed for the liquids in Paulsen *et al.* (2011) with viscosities $\mu = 3.3, 48, 230$ mPa s as for these mixtures σ and ρ vary least ($\rho = 1200$ kg m⁻³ and $\sigma = 65$ mN m⁻¹). (The required information about the mixtures was provided to us by Dr J. D. Paulsen, Dr J. C. Burton and Professor S. R. Nagel.) For the chosen mixtures, one has $Re = 1.4 \times 10^4, 68, 2.9$. To elucidate the role of the gas’ viscosity, we will look at the difference between the coalescence occurring in a passive gas studied earlier (Sprittles & Shikhmurzaev 2012a) and, as in experiments, in air of density $\rho_g = 1.2$ kg m⁻³ and viscosity $\mu_g = 18$ μ Pa s. Then, the gas-to-liquid density ratio is $\bar{\rho} = 10^{-3}$ and the viscosity ratios are, respectively, $\bar{\mu} = 5.5 \times 10^{-3}, 3.8 \times 10^{-4}, 7.8 \times 10^{-5}$.

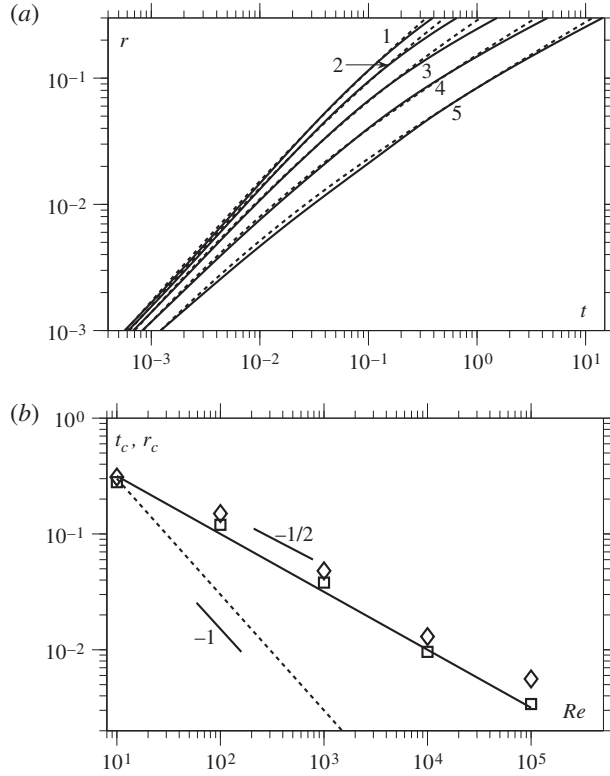


FIGURE 14. Effect of the Re , with $\bar{\mu} = 4.6 \times 10^{-5} Re^{1/2}$ for the case of a varying viscosity: curve 1, $Re = 10$; curve 2, $Re = 10^2$; curve 3, $Re = 10^3$; curve 4, $Re = 10^4$; and curve 5, $Re = 10^5$. Dashed lines are (7.2) with constants that are plotted in the lower figure: diamonds are t_c and squares are r_c .

Importantly, as one can clearly see in figure 15, over the range of viscosities considered, the presence of the gas does slow down the evolution of the bridge front (curves 2), as compared with the case of a passive gas (curves 1), but this effect is not sufficient to account for the discrepancy between the conventional model's predictions and the experimental data from Paulsen *et al.* (2011) over the entire period of the experiment. In particular, although the gas viscosity slows the speed of the initial motion down, even for the relatively high-viscosity liquid drops, the conventional model still overshoots the data for the initial stages of the experiment.

It is interesting to see that, roughly, the magnitude of the effect which the introduction of a viscous gas has on the bridge evolution is the same across two orders of magnitude in liquid viscosity. The reason is that although the viscosity ratio with air decreases with increasing liquid viscosity, the Reynolds number also decreases and, as shown in § 6.3.3, this results in the gas' influence becoming larger. These two opposing effects appear to approximately balance each other.

8. Discussion

Consider now what has been learnt about the initial stages of bridge propagation described in the framework of the conventional model and how this ties in with previously published experimental and computational studies.

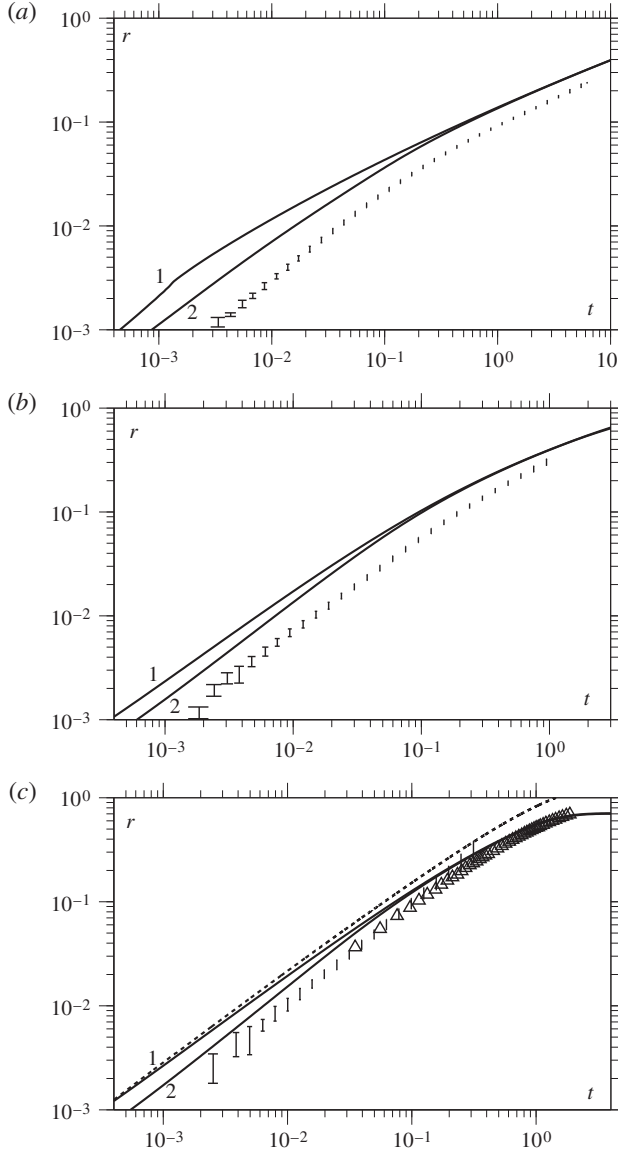


FIGURE 15. The time-dependence of the radius of the liquid bridge connecting the coalescing drops obtained in the framework of the conventional model: curve 1, the drops are in a passive gas; curve 2, the ambient gas is viscous with $(Re, \bar{\mu}) = (1.4 \times 10^4, 5.5 \times 10^{-3})$ in (a), $(68, 3.8 \times 10^{-4})$ in (b) and $(2.9, 7.8 \times 10^{-5})$ in (c). The dashed line in (c) corresponds to (2.1). The error bars are from experiments in Paulsen *et al.* (2011), and the triangles are from optical observations in Thoroddsen *et al.* (2005).

8.1. The presence of an ILV regime for $Re \leq 1$

It has been shown that for a passive gas, the Stokes flow solution (2.1) describes the initial stages of growth for $Re \leq 1$, a result that is in direct conflict with the conclusions of Paulsen *et al.* (2012) which claim that the Stokes flow solution is only entered after the ILV regime has occurred. In Paulsen *et al.* (2012), a key observation

in favour of the ILV regime is that, at finite Re , it takes a certain time for the apex of the drop to follow the Stokes flow solution, and we have also observed this phenomenon. How then, do these apparently contradictory findings square with each other?

First, the computations performed in Paulsen *et al.* (2012), see for example figure 3E there, are for $r > 10^{-2}$ which only leaves the interval $10^{-2} < r < 10^{-1}$ to consider the initial stage of motion. Consequently, the good agreement of Hopper's solution (2.1) with full computations at $Re \sim 1$, for $r \ll 1$, confirmed here in figure 15 for exactly the same case as that in figure 3E of Paulsen *et al.* (2012), appears to have been missed. Instead, in Paulsen *et al.* (2012), the results of the computations are shown to give an approximately linear growth in the bridge radius and this is used as evidence against the Stokes regime. We have seen that this is not the case. For $Re \leq 1$, $\bar{\mu} = 0$ and $r \ll 1$, the bridge propagation is best described by Hopper's solution (2.1) corresponding to the Stokes regime.

Far from the bridge front, at finite Re , the inertia is important as the flow then takes some time to develop, in contrast to the $Re = 0$ case. Thus, if one considers the global motion of the drops for $Re \leq 1$, it makes sense to talk of an ILV regime, even though local to the bridge front the finiteness of Re has a negligible effect.

Second, we would like to tie these observations in with the experimental findings in Paulsen *et al.* (2011, 2012). This is quite tricky, as it involves considering the effect of the gas on the motion as well as recognising that quantitatively the experiments do not agree well with the predictions of the conventional model (figure 15). One thing that can be noted; however, is that there has been no systematic experimental investigation of the regime $Re \leq 1$ and $r \ll 1$. In Paulsen *et al.* (2011) the electrical measurements allowed for $r \ll 1$, but all data was for $Re \geq 1$, whilst in Paulsen *et al.* (2012) hanging pendent drops of huge viscosity were considered, so that $Re \leq 1$, but only optical measurements were made, so that $r > 0.1$. Further experiments on this regime may reveal more details about the initial stages of motion.

8.2. Characterising parameter space

Much has been made about the different 'regimes' of coalescence, their different 'scalings' and the possibility of collapsing all data onto a master curve using two fitting parameters. However, let us consider instead the question of when such simplified models actually allow us to ascertain accurate quantitative information about the coalescence event. First, such data about the entire drop shape is impossible, as it is only in the two-dimensional case that the theory of Hopper (1984) applies, and the other works all consider only predictions for the bridge radius as a function of time, i.e. 'local' information. Moreover, to increase our chances of progress in this task, let us further simplify matters by considering the gas to be passive, so that the only governing parameter is then the Reynolds number. So the question essentially becomes, at a given Re , at what bridge radii r is there a quantitative formula which relates r to time t ?

This question has been addressed in previous works, e.g. Paulsen *et al.* (2012), but the difference between their approach and the one we take here is that we are interested in where quantitative predictions can be made, rather than where qualitative behaviour occurs. Mathematically, the difference is that, whilst previous works have put all coalescence events where the bridge radius scales in a certain way, e.g. linear $r = C_v t$, into one regime, with C_v fitted to the data in an arbitrary way, here, we will only consider regimes in which there are no fitted prefactors, e.g. (2.1), or those in

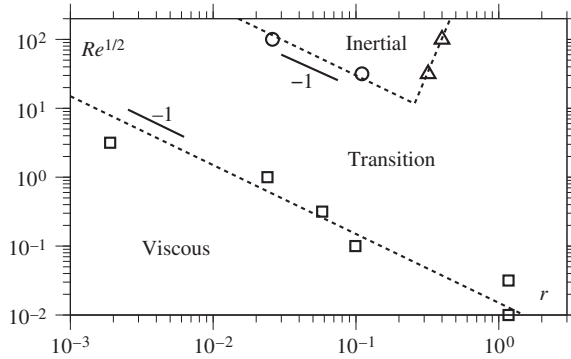


FIGURE 16. Phase diagram showing the regions in which the bridge radius r is in the viscous regime described by (2.1) or in the inertial regime described by (2.4) with $C_i = 1.5$. Dashed lines are rough fits to the data with the lower dashed line given by $Re^{1/2} = 1.5 \times 10^{-2} r^{-1}$, upper dashed line (with gradient -1) is $Re^{1/2} = 3r^{-1}$ and the third dashed line, going through the triangles, is simply to guide the eye.

which the prefactor is known and fixed. This is not a better approach than Paulsen *et al.* (2012), it is just a different one, motivated by a desire to understand in which parts of parameter space quantitative predictions using simple analytic formulas can be made.

To be precise, consider the error $E(t)$ between a computed solution $r(t)$ and an approximate expression $r_{approx}(t)$ to be given by

$$E = \frac{|r - r_{approx}|}{r} \quad (8.1)$$

and consider, for a given Re , the values of the radius r for which relative error falls below 10 % ($E < 0.1$), i.e. very crudely, below experimental error. The result will be that for each r_{approx} there is a section of (Re, r) phase space in which the approximate expression meets the required tolerance. As with the computations, only $r > 10^{-3}$ is considered, as before this point there are large relative errors associated with the finite initial bridge radius from which the computations start.

In figure 16, the new phase diagram is shown which, to be consistent with previous works, has been produced for the case of free spheres coalescing. A phase diagram for pinned hemispheres differs very little, as it is only in the later stages of motion, $r > 0.1$, that geometry starts to have an effect. It makes sense to plot r against $Re^{1/2}$ rather than Re as (a) we see that the boundaries to the different regions of phase space are given by $r \propto Re^{-1/2}$ and (b) by flipping the curves about the plane $Re = 1$, the plot becomes r versus $Oh = Re^{-1/2}$ so that a comparison with the phase diagram in Paulsen *et al.* (2012) can more easily be performed.

Square markers show the region in which Hopper's solution (2.1) accurately describes the computed solutions to within the required tolerance. These quantitative results confirm that, in the initial stages of motion, the Stokes flow solution describes the bridge's dynamics for a distance $r = r(Re)$ and that this distance scales like $Re^{-1/2}$. Exiting the viscous regime does not mean that the motion is then in an inertial regime. In actual fact, there is a large part of parameter space where the motion can neither be considered viscosity-dominated nor inertia-dominated. Although it is tempting to call this the ILV regime, and in some sense it is, as it is the region where inertial

and viscous forces are important, we have labelled this region ‘transition’ as, to be consistent with our aims, there is no quantitative predictive expression for this region, and all what we know is that the process goes across this regime from ‘viscous’ to ‘inertial’.

For high enough Re , roughly $Re > 100$, an inertial regime is entered in which (2.4) with $C_i = 1.5$ accurately describes the computed solution. Notably, this region has both a lower bound, as it takes some distance for viscous effects to become negligible, and an upper bound at which point the assumptions made in (2.4), such as the motion being driven entirely by the longitudinal curvature, no longer hold, see Sprittles & Shikhmurzaev (2014b) for further details.

The phase diagram we have created can be very simply interpreted. In the viscous region, the motion can be approximated by the Stokes equations, i.e. neglecting the inertial terms, whilst in the inertial regime the viscous terms are negligible, so that the Euler equations should be able to describe the motion. Elsewhere the full Navier–Stokes equations are necessary for accurate computation and thus simplified expressions based on the aforementioned limiting cases cannot in principle be accurate.

The computed two-dimensional phase diagram is actually a cross-section ($\bar{\mu} = 0$) of the three-dimensional parameter space $(r, \sqrt{Re}, \bar{\mu})$ which would be required if the viscosity ratio was also accounted for. At moderate $\bar{\mu}$, it is likely that Hopper’s solution will no longer become an accurate representation of the initial stages, so that no currently available quantitative expressions exist for this period. It may be that in this case, a linear expression, as proposed in Paulsen *et al.* (2011), describes the data well, but that the required prefactor’s dependency on Re and $\bar{\mu}$ will be *a priori* unknown. Thus, in this situation, the region in which computations are required to provide quantitative predictions of the coalescence phenomenon will inevitably grow.

9. Outlook

Using computational techniques, a systematic parametric study of the process of coalescence in the framework of the conventional model has been performed and has enabled us to identify a number of misconceptions in the published literature and suggest avenues of further research.

In particular, our results have shown the following.

- (a) When viscous forces dominate inertial ones, Hopper’s solution (Hopper 1984) best approximates the initial stages of coalescence local to the bridge front and the ILV regime is seen to be a characteristic of the global motion of the drops. In contrast, experimental results in Paulsen *et al.* (2012), Paulsen (2013), Paulsen *et al.* (2014) indicate that this regime also affects the local motion of the bridge front. The reason for this discrepancy remains unexplained.
- (b) There is a ‘transition region’ in which, currently, there is no predictive analytic theory.
- (c) Toroidal bubbles are not formed for coalescence of liquid drops in air at atmospheric pressure.
- (d) The conventional model captures the scaling behaviour of the transitions between different regimes observed in experiments, but quantitatively overshoots the data for r versus t .

Each of these findings suggests a particular avenue of enquiry deserving of further attention.

- (a) Electrical methods focused on the very initial stages of coalescence for high-viscosity liquids (low Re) would determine whether or not experimental measurements agree with the conventional model's prediction that this regime can be described by Hopper's solution.
- (b) If it is possible to develop an asymptotic theory for the transition regime, that gives a simplified framework into which the predictions of the conventional model can be understood, much like Hopper's solution for the viscous regime, then this should be considered and our results would provide a benchmark for it. If not, as seems likely, particularly when considering the influence of an ambient fluid as well, then computational techniques should be recognised as the only approach giving quantitative predictions for this regime.
- (c) To attempt to reach the regime in which toroidal bubble formation can be observed, one must consider lowering the influence of the gas viscosity. This could potentially be realised by reducing the ambient pressure of the gas. Simulations in this regime may shed further light on this possibility and thus aid any experimental attempts.
- (d) Perhaps most importantly, experimental and theoretical aspects of the coalescence process should be reconsidered in light of the poor quantitative agreement between electrical measurements and the predictions of the conventional model. Two possibilities for the discrepancy are that (i) there is an effect in the experiment which is not accounted for in the theory, such as the influence of the electric field on the motion or (ii) that the conventional model itself is unable to capture the initial stages of motion due to its singular nature, and, if this is the case, then singularity-free descriptions that incorporate extra physics, such as the interface formation model considered in Sprittles & Shikhmurzaev (2012a, 2014a), deserve further attention.

Acknowledgements

The authors would like to thank Dr J. D. Paulsen, Dr J. C. Burton and Professor S. R. Nagel for providing us with the data from their experiments published in Paulsen *et al.* (2011, 2012).

REFERENCES

- AARTS, D. G. A. L., LEKKERKERKER, H. N. W., GUO, H., WEGDAM, G. H. & BONN, D. 2005 Hydrodynamics of droplet coalescence. *Phys. Rev. Lett.* **95**, 164503.
- DERBY, B. 2010 Inkjet printing of functional and structural materials: fluid property requirements, feature stability and resolution. *Annu. Rev. Mater. Res.* **40**, 395–414.
- DUCHEMIN, L., EGGERS, J. & JOSSEMAND, C. 2003 Inviscid coalescence of drops. *J. Fluid Mech.* **487**, 167–178.
- EDDI, A., WINKELS, K. G. & SNOEIJER, J. H. 2013 Short time dynamics of viscous drop spreading. *Phys. Fluids* **25**, 013102.
- EGGERS, J., LISTER, J. R. & STONE, H. A. 1999 Coalescence of liquid drops. *J. Fluid Mech.* **401**, 293–310.
- ENRIGHT, R., MILJKOVIC, N., AL-OBEIDI, A., THOMPSON, C. V. & WANG, E. N. 2012 Condensation on superhydrophobic surfaces: the role of local energy barriers and structure length scale. *Langmuir* **28**, 14424–14432.
- HOPPER, R. W. 1984 Coalescence of two equal cylinders: exact results for creeping viscous plane flow driven by capillarity. *J. Am. Ceram. Soc.* **67**, 262–264.

- HOPPER, R. W. 1990 Plane Stokes flow driven by capillarity on a free surface. *J. Fluid Mech.* **213**, 349–375.
- HOPPER, R. W. 1993a Coalescence of two viscous cylinders by capillarity: part 1. Theory. *J. Am. Ceram. Soc.* **76**, 2947–2952.
- HOPPER, R. W. 1993b Coalescence of two viscous cylinders by capillarity: part 2. Shape evolution. *J. Am. Ceram. Soc.* **76**, 2953–2960.
- MENCHACA-ROCHA, A., MARTÍNEZ-DÁVALOS, A., NÚÑEZ, R., POPINET, S. & ZALESKI, S. 2001 Coalescence of liquid drops by surface tension. *Phys. Rev. E* **63**, 046309.
- OGUZ, H. N. & PROSPERETTI, A. 1989 Surface-tension effects in the contact of liquid surfaces. *J. Fluid Mech.* **203**, 149–171.
- PAULSEN, J. D. 2013 Approach and coalescence of liquid drops in air. *Phys. Rev. E* **88**, 063010.
- PAULSEN, J. D., BURTON, J. C. & NAGEL, S. R. 2011 Viscous to inertial crossover in liquid drop coalescence. *Phys. Rev. Lett.* **106**, 114501.
- PAULSEN, J. D., BURTON, J. C., NAGEL, S. R., APPATHURAI, S., HARRIS, M. T. & BASARAN, O. 2012 The inexorable resistance of inertia determines the initial regime of drop coalescence. *Proc. Natl Acad. Sci. USA* **109**, 6857–6861.
- PAULSEN, J. D., CARMIGNIANI, R., KANNAN, A., BURTON, J. C. & NAGEL, S. R. 2014 Coalescence of bubbles and drops in an outer fluid. *Nat. Commun.* **5**, 3182.
- RICHARDSON, S. 1992 Two-dimensional slow viscous flows with time-dependent free boundaries driven by surface tension. *Eur. J. Appl. Maths* **3**, 193–207.
- SHIKHMURZAEV, Y. D. 2007 *Capillary Flows with Forming Interfaces*. Chapman & Hall/CRC.
- SPRITTLES, J. E. & SHIKHMURZAEV, Y. D. 2012a Coalescence of liquid drops: different models versus experiment. *Phys. Fluids* **24**, 122105.
- SPRITTLES, J. E. & SHIKHMURZAEV, Y. D. 2012b The dynamics of liquid drops and their interaction with solids of varying wettabilities. *Phys. Fluids* **24**, 082001.
- SPRITTLES, J. E. & SHIKHMURZAEV, Y. D. 2012c A finite element framework for describing dynamic wetting phenomena. *Intl J. Numer. Meth. Fluids* **68**, 1257–1298.
- SPRITTLES, J. E. & SHIKHMURZAEV, Y. D. 2013 Finite element simulation of dynamic wetting flows as an interface formation process. *J. Comput. Phys.* **233**, 34–65.
- SPRITTLES, J. E. & SHIKHMURZAEV, Y. D. 2014a The coalescence of liquid drops in a viscous fluid: interface formation model. *J. Fluid Mech.* **751**, 480–499.
- SPRITTLES, J. E. & SHIKHMURZAEV, Y. D. 2014b Dynamics of liquid drops coalescing in the inertial regime. *Phys. Rev. E* **89**, 063006.
- THORODDSEN, S. T., ETOH, T. G. & TAKEHARA, K. 2008 High-speed imaging of drops and bubbles. *Annu. Rev. Fluid Mech.* **40**, 257–285.
- THORODDSEN, S. T. & TAKEHARA, K. 2000 The coalescence cascade of a drop. *Phys. Fluids* **12**, 1265–1267.
- THORODDSEN, S. T., TAKEHARA, K. & ETOH, T. G. 2005 The coalescence speed of a pendent and sessile drop. *J. Fluid Mech.* **527**, 85–114.
- WU, M., CUBAUD, T. & HO, C. 2004 Scaling law in liquid drop coalescence driven by surface tension. *Phys. Fluids* **16**, 51–54.